In Vivo 3D Spatial/1D Spectral Imaging by Spatiotemporal Encoding: A New Single-Shot Experimental and Processing Approach

Rita Schmidt and Lucio Frydman*

A novel method for acquiring and processing quality multislice spectroscopically resolved 2D images in a single shot is introduced and illustrated. By contrast to the majority of single-scan spectroscopic imaging sequences developed so far, the method here discussed is not based on the acquisition of echo planar data in the k/t-space, but rather on the use of recently proposed spatiotemporal encoding methods. These techniques provide a robust alternative to classical techniques, as they can scan two spatial plus one spectral dimension by oscillating a single imaging gradient. This work demonstrates that the use of extended spectral/spatial super-resolution algorithms coupled to new experimental spatiotemporal encoding formulations based on swept inversions rather than on chirped excitations can lead to novel spatiotemporal encoding-based tools for resolving complex multisliced 2D images according to the chemical shifts in subsecond experiments. A number of phantom-based models were explored to clarify the relative merits of this technique and estimate its sensitivity performance. In vivo results of fat and water separation on abdominal imaging of mice at 7 T and on human breast imaging at 3 T are presented. **Magn Reson Med 70:382–391, 2013. © 2012 Wiley Periodicals, Inc.**

Key words: spatiotemporal encoding; single-shot acquisitions; spectroscopic imaging; extended spectral/spatial super-resolution; in vivo water/fat imaging

INTRODUCTION

Spectroscopic imaging techniques play a large number of roles in contemporary research (1–5). Further interest has been triggered on these experiments over the last years with new demands for fast spectroscopic imaging tools given by the advent of hyperpolarization-based forms of molecular imaging (6–8). One of the challenges raised by spectroscopic imaging methods rests in their high-intrinsic dimensionality, which in principle entails three spatial axes in addition to a fourth spectroscopic axis (9). Usual methods monitoring multiple indirect-domains in a scan-by-scan fashion may lead to unacceptably long experimental times; high-speed imaging strategies like echo-planar imaging (EPI; Ref. 10) can play an important role in alleviating such acquisition time problems. Particularly promising are gradient-echoing approaches that rapidly scan k-space while allowing shifts to develop along an inherently "slow" spectroscopic acquisition dimension. These concepts underlie echo planar spectroscopic imaging (EPSI, Refs. 2,11–13), which involving either Cartesian or "zig-zag" k/t-scanning forms arguably provide the most widely used approach to accelerated spectroscopic imaging today. Even EPSI echo trains, however, face limitations stemming from their need to rapidly oscillate the spatial gradients over the course of each dwell time in the spectroscopic acquisition: with one oscillatory loop needed per spatially encoded dimension, limited acceleration factors can be imparted in this fashion before compromising on the ensuing spectrum's width. Other fast-scanning techniques based on principles that differ from EPSI, as well as combinations of EPSI with segmented and parallel imaging approaches, have consequently been proposed and demonstrated (14–17). Counting among the EPI alternatives is a recent proposal for performing ultrafast imaging in multiple dimensions, using what we shall refer to as spatiotemporal encoding (SPEN) principles. In these methods, closely related to quadratic phase excitation approaches first discussed in imaging contexts by Kunz and Pipe (18,19), spins are excited sequentially in space—for instance with the aid of a frequency-chirped 90° radiofrequency (RF) pulse (20). Their response is likewise monitored in a spatially and temporally resolved fashion during the acquisition, leading to the spins' delivering the spatial profile being sought directly in their time-domain amplitude response. Imaging information can, therefore, arise from a magnitude-mode calculation of the free induction decay (FID) signal—without the need for an additional Fourier transform (FT) of the data. An interesting feature of the resulting approach then stems from the fact that, whereas the FID's amplitude carries information about the spins' spatial distribution, its phase modulation can convey the chemical shift offset of the ensuing emitting sites. This information is actually built-in into SPEN experiments, i.e., it is encoded at no extra cost in the experiment's complexity, without the need to impose an additional echo-planar oscillation of the spatially encoding gradient. Whereas such offset-conveying information may not be relevant if the compound being imaged solely involves water, its measurement becomes important within the context of spectroscopic imaging. Tal and Frydman (21)
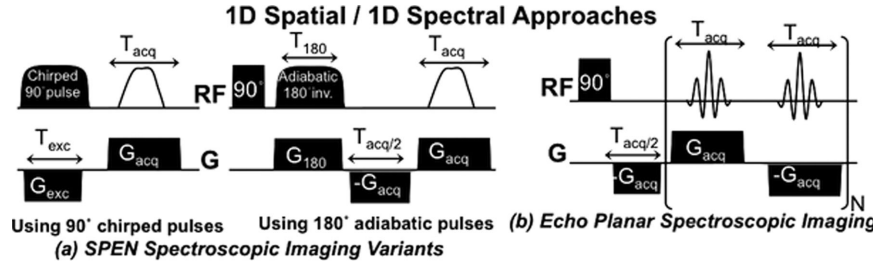
FIG. 1. Survey of 1D spectroscopic and 1D spatial imaging single-scan schemes. **a:** Non-FT scheme for spatial plus spectral encoding incorporating 90° chirped excitation (left) or adiabatic 180° inversion/refocusing (center) pulses. **b:** Echo-planar spectroscopic imaging (EPSI) approach to extract spatial / spectral correlations.

discussed a postprocessing possibility to recover such additional chemical shift dimension based on a filtering procedure that, although not affecting or imposing additional demands on the nature of the actual 2D SPEN imaging acquisition, could compromise the ensuing spatial resolution. Its performance was then demonstrated for water/dimethylsulfoxide and water/chloroform phantoms.

Although clearly demonstrative of the approach's capability to encode both spatial and spectral information, this original proposal required further optimizations to become relevant as a practical spectroscopic imaging approach in preclinical or clinical settings. Two particularly important handicaps to be resolved included the spatial resolution issue just mentioned and the reliance of the original sequence on an initial 90° chirped excitation of the spins, which complicated the acquisition of multislice spectroscopic images. The aim of this work is to introduce a number of provisions capable of dealing with these limitations, to alleviate the relatively high specific absorption rate (SAR) that would have resulted from the original proposals, and to illustrate the ensuing capabilities to obtain quality volumetric spectroscopic images in subsecond timescales. These illustrations are presented here for both in vitro phantoms to assess various image-, spectral-, and sensitivity-quality issues, as well as with in vivo demonstrations aimed at illustrating the method's ultrafast spectroscopic imaging abilities in preclinical and clinical settings. Toward this end, we begin by reviewing in the next section the basic physics of the method, as well as progress made possible by the introduction of adiabatic 180° RF sweeps and of super-resolution (SR) postprocessing techniques (22), to alleviate the resolution, the SAR and the multislicing challenges mentioned above. We then proceed to illustrate the implementation of the chemical sites separation method using SPEN on metabolites in vitro, as well as in vivo with 2D spatial/1D spectral single-scan multislice experiments of mice abdomen at 7 T and of human breast scans at 3 T. These different experimental sets demonstrate the method's abilities to target a range of frequency shift separations, different concentrations and varying number of spectral peaks—always while retaining high spatial resolution characteristics. Further potential improvements of the method and a variety of uses are then briefly discussed.

METHODS

Resolving Chemical Shift Information in SPEN Imaging: Principles and an Extended SR Formulation

To summarize the way by which SPEN can deliver, at the same time, both spatial and spectroscopic aspects about the spins' evolution, we consider the simplest 1D form of quadratic encoding illustrated in Figure 1a. This involves an RF-driven excitation of the spins based on a chirped 90° pulse acting in the presence of an excitation gradient G_{exc}, followed by a signal readout under the action of a decoding acquisition gradient G_{acq}. The range of the sweep $\gamma G_{exc} FOV$ defines the maximum observed field of view (FOV), and the excitation/acquisition times are tuned to enable the full read-out of the encoded information by fulfilling $G_{exc} T_{exc} = -G_{acq} T_{acq}$. Assuming the encoding occurs along the y dimension on a site with chemical shift offset ω_{CS}, the initial excitation will impart the spins with a quadratic phase

$$\phi_{exc}(y) = \frac{\gamma G_{exc} T_{exc}}{2FOV} y^2 + \left(\frac{\gamma G_{exc} T_{exc}}{2} - \frac{\omega_{CS} T_{exc}}{FOV} \right) y + \text{const.}$$

[1]

Subsequent acquisition under a wavenumber $k(t) = \gamma \int_0^t G_{acq}(t') dt'$ acting over the acquisition time t, results on a FID signal

$$S(t) \propto \Delta y$$
$$\cdot \rho_{\omega_{cs}}(y_{k(t)}) \exp \lfloor i \{ \varphi_{exc}(y_{k(t)}) + k(t) \cdot y_{k(t)} + \omega_{CS} t \} \rfloor.$$

[2]

Here Δy is a nominal spatial resolution defined during the encoding by $\Delta y = \sqrt{\frac{FOV}{\gamma G_{exc} T_{exc}}}$, and $\rho_{\omega_{cs}}$ is the spatial density image being sought for this particular chemical site. The focal, highest-sensitivity point of the resulting acquisition is then unraveled on a t-dependent basis according to the decoding condition

$$y_{k(t)} = \left(\frac{FOV}{2} - \frac{\omega_{CS}}{\gamma G_{exc}} \right) - \frac{FOV}{T_{acq}} \cdot t$$

[3]

The linear $\omega_{CS} \cdot t$ term modulating the FID in Eq. [2] implies that the sample's chemical shift spectrum can arise from a FT of the signal, provided that the remaining terms are accounted for. As all these remaining exponential terms are given by a series of parameters that are both known a priori and common

to all chemically shifted sites in the sample, they can be removed by suitable postprocessing of the FID. In fact multiplying the time-domain signal $S(t)$ on a point-by-point basis by a suitable gradient-dependent conjugate phasor

$$S'(t) = \exp\left[-i\left(\frac{\gamma G_{\text{acq}}\text{FOV} \cdot T_{\text{exc}}}{2T_{\text{acq}}^2}t^2 - \frac{\gamma G_{\text{acq}}\text{FOV} \cdot T_{\text{exc}}}{2T_{\text{acq}}}t\right)\right]$$
$$\cdot S(t) \propto \sum_{\text{CS}} \rho_{\omega_{\text{cs}}}(y_{k(t)}) \exp\left[i\left(1 - \frac{G_{\text{acq}}}{G_{\text{exc}}}\right)\omega_{\text{CS}}t\right]$$

[4]

leads to a usual-looking spectroscopic FID, described in Eq. [4]'s right-hand side under the assumption of multiple CS-shifted sites. With the acquired signal thus modified, Tal and Frydman (21) described a simple series that could yield, for each chemically shifted site, its corresponding spin density image as follows: (i) calculate the modified signal $S'(t)$; (ii) obtain by Fourier-transform of it the 1D sample's nuclear magnetic resonance spectrum resolving every chemical shifted peak; (iii) separate the individual contributions arising from each ensuing chemical-shifted site by applying a suitable spectral filtering, and (iv) inverse FT each of these filtered peaks to reconstruct—by calculating the magnitude mode of the resulting signals—each chemical site's SPEN image (the phasor multiplication leading from $S(t)$ to $S'(t)$ having no effect upon doing such calculation). Notice that unlike what happens with the EPSI sequence (Fig. 1b), such procedure can result on an array of spectrally resolved spatial images without the need of oscillating the imaging gradient.

A main drawback of the original SPEN formulation vis-à-vis normal k-based imaging, rested in the former's lower spatial resolving power per unit gradient strength (20). For a given set of imaging acquisition parameters T_{acq}, Δy, and FOV, SPEN's gradient demands would be $\sqrt{(\text{FOV}/\Delta y)}$ times larger than those of its EPSI counterpart. In actuality, however, a large redundancy of digitized information would then characterize the signal. As discussed in Ref. 22, it is possible to exploit this redundancy using SR formalisms, which go beyond retrieving the sought image from a simple magnitude calculation. In the original, single $\omega_{\text{CS}} = 0$ site implementation of this algorithm, this was exploited by recasting the discrete digitized form of Eq. [2] as a system of linear equations

$$\left\{\vec{S}(t_i) = \sum_{k=1}^{M} \overline{\overline{A}}(t_i, y_k)\vec{\rho}_{\text{SR}}(y_k)\right\}_{i=1,\dots,N}$$

[5a]

$$\begin{pmatrix} S(\Delta t) \\ S(2\Delta t) \\ \vdots \\ S(N\Delta t) \end{pmatrix} = \begin{pmatrix} A(\Delta t, y_1) & A(\Delta t, y_2) & \cdots & A(\Delta t, y_M) \\ A(2\Delta t, y_1) & A(2\Delta t, y_2) & \cdots & A(2\Delta t, y_M) \\ \vdots & \vdots & \ddots & \vdots \\ A(N\Delta t, y_1) & A(N\Delta t, y_2) & \cdots & A(N\Delta t, y_M) \end{pmatrix}$$
$$\cdot \begin{pmatrix} \rho(y_1) \\ \rho(y_2) \\ \vdots \\ \rho(y_M) \end{pmatrix}$$

[5b]

and subsequently solving for $\{\vec{\rho}_{\text{SR}}(\underline{y}_k)\}_{k=1,M}$ by standard minimization methods. Herein the $\overline{A}$ matrix contains the phase encoding arising from the SPEN manipulation, and relates the N number of points acquired in the time-domain, with the M number of the points desired along the spatial dimension. As M is usually large enough to fulfill $M > (\text{FOV}/\Delta y)$, an improved spatial resolution could be achieved in this fashion at no extra penalty. To exploit SPEN's full spectroscopic imaging potential, this SR formulation is here extended to the reconstruction of spatially resolved images from multiple chemically shifted sites. To do so, we assume that the acquired signal (Eq. [2]) is proportional to the sum of spin densities arising from all Q chemical sites potentially contributing to the sample's spectrum, and its phase modulation reflects both the quadratic y^2 dependence coming from the spatial encoding and an additional linear chemical shift phase modulation. Taking into account the discrete nature of the digitized SPEN signal, of the spatial image being sought and of the chemical shift spectrum, enables one to recast this problem algebraically as

$$\left\{\vec{S}(t_i) = \sum_{q=1}^{Q} \vec{S}_q(t_i) = \sum_{q=1}^{Q}\left\{\sum_{k=1}^{M} \overline{\overline{A}}(t_i, y_k, \omega_{\text{CS}}^q)\vec{\rho}^{\,q}(y_k)\right\}\right\}_{i=1,\dots,N}$$

[6]

which describes each chemical site's spin densities $(\rho^1\dots\rho^Q)$ as a (potentially super-resolved) spatially dependent vector of its own. Combining these Q individual contributions in a single column vector of dimension $Q\cdot M$, it is possible to recast Eq. [6] into a multisite system of linear equations

$$\left\{\vec{S}(t_i) = \left(\vec{S}_1(t_i) \;\; \vec{S}_2(t_i) \;\; \cdots \;\; \vec{S}_Q(t_i)\right) \cdot \begin{pmatrix} 1 \\ 1 \\ \vdots \\ 1 \end{pmatrix}\right.$$
$$\left. = \left(A_1(t_i, y_k) \;\; A_1(t_i, y_k) \;\; \cdots \;\; A_Q(t_i, y_k)\right) \cdot \begin{pmatrix} \rho^1(y_k) \\ \rho^2(y_k) \\ \vdots \\ \rho^Q(y_k) \end{pmatrix}\right\}_{i=1,\dots,N}$$

(7)

where $(1\dots1)$ is an all-ones vector of dimension $Q\cdot M$, and the $A_1\dots A_Q$ are matrices akin to those in Eq. [5]—possessing identical spatial point spread functions but differing by their chemical shift evolution phasors, as given in the right-hand side of Eq. [4]. Figure 2 illustrates the kind of properties adopted by the resulting "extended" A_{ext} block-diagonal matrix for two chemical sites (e.g., fat and water at 3 T) in terms of the magnitude and phase of its components. The latter linear phase modulations along y, which were absent in the original SPEN treatment dealing solely with a single on-resonance chemical site, encompass the effects of shifts introduced by the presence of multiple inequivalent chemical sites.

Equation [7] can often be inverted to get a description of the spatial densities $\rho_{\text{ext}}(y) = [\rho^1(y)\dots\rho^Q(y)]$, characterizing
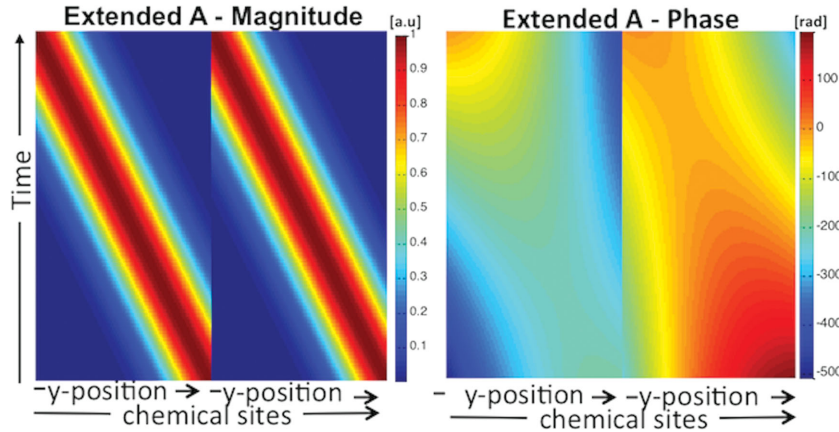
FIG. 2. Example of the extended A_{ext} matrix (Eq. [7]) for two chemical sites, illustrating the magnitude (left) and the phase (right) dependencies of the matrix elements. [Color figure can be viewed in the online issue, which is available at wileyonlinelibrary.com.]

the spatial distribution of every chemical component in the sample. For instance the least squares criterion

$$\rho_{ext} = \left(A_{ext}^{+} \cdot A_{ext}\right)^{-1} \cdot A_{ext}^{+} \cdot S \qquad [8]$$

based on finding A_{ext}'s pseudoinverse matrix A_{ext}^{+} with the aid of an iterative regularization procedure, can yield a well-defined image description provided that the number of digitized signal points N is equal or larger than the number of points $M \times Q$ sought for the combined super-resolved vector $[\rho_1 \ldots \rho_Q]$. Given, however, that the conditioning of the inversion problem associated to the passage from Eq. [7] to [8] is fairly well behaved, a simpler, noniterative solution using the conjugate gradient method suggested in Ref. 22, can also be used. This involves applying a gaussian weighting on the A_{ext} matrix, and performing a single iteration of the form

$$\rho_{ext} = \left(A_{ext}^{weighted}\right)^{+} \cdot S \qquad [9]$$

This was found to give good results also in the present spectroscopically resolved case—even if it meant that given a fixed number of sampled data points N, a best fit reconstruction of the spatial images arising from each chemical site had to proceed at the expense of reducing the number of points in each image vector by a factor Q. This is similar to what was shown to be the case in Refs. 21 and 22 using the filtering method. Yet this will not necessarily always be the limiting case when processing spectroscopic imaging data using the SR approach; for example, when the signal is sparse and/or the difference between the relevant shifts is a priori known (as is often the case when dealing with fat and water), resolution can be improved without sacrifices in the stability of the inversion problem. We consequently found super-resolved solutions stemming from Eq. [9]'s minimization to yield equal or better spectral and spatial results than their filtering-derived counterparts. Results obtained using the previously suggested filtering/magnitude calculation method versus the new suggestion given herein, are further compared later.

Pulse Sequencing Considerations

Previous SR-oriented SPEN studies were often based on applying a quadratic spatial encoding on the spins via a sequential excitation imparted by a frequency-chirped 90° pulse. To facilitate multislice acquisitions, however, this study relied on sequences that started with a fixed-frequency 90° slice-selective excitation pulse, and imparted the quadratic spatial encoding sought with a subsequent 180° inversion chirp applied in the presence of an encoding gradient (Fig. 1a, center). While such combination can impart on the targeted slice a parabolic phase profile, the use of an inversion pulse will take as well all remaining spins in the sample away from equilibrium. This effect was counteracted by the introduction of a second, nonselective 180° inversion pulse, akin to that described in Ref. 23 but of a "hard" rather than a "chirp" rewinding character. Although several, equally valid choices could be selected for placing such 180° pulse, Figure 3 shows the version that ended up giving an optimum experimental performance in this study. The remaining of the sequence shown in this figure is of the typical "hybrid" character, where SPEN replaces what would usually be EPI's phase-encoding dimension ("y"), and a readout direction ("x") is encoded as is usual in magnetic resonance imaging in the corresponding k-domain. Features worth noticing about the resulting sequence include

- a reliance on 180° inversions, which will change the actual chemical shift modulation from the form given in Eq. [4] to $S'(t)$
  $$\propto \sum_{Q} \rho^{Q}(y) exp\left[i\left(1 - \frac{G_{acq}}{2G_{180}}\right)\omega_{CS}t\right]$$
- the sequence's introduction of additional delays between the pulses, capable of defining the exact echoing timing for arbitrary chirped pulse and acquisition durations, T_{180} and T_{acq}, respectively
- the sequence's need for a sufficiently long acquisition time to resolve among chemically inequivalent peaks as given by $T_{acq} > \frac{2G_{180}}{(2G_{180} - G_{acq})\Delta\nu}$ (where T_{acq} is a physical evolution time that also takes into account the period taken by the readout decoding).

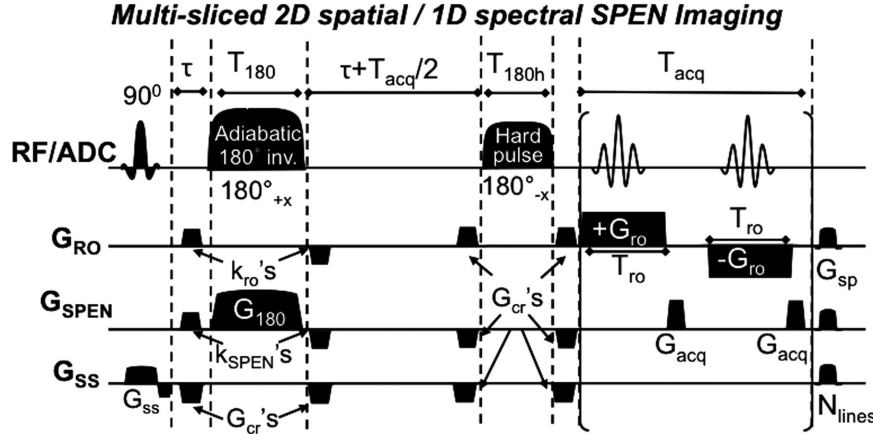**Multi-sliced 2D spatial / 1D spectral SPEN Imaging**

FIG. 3. Multisliced hybrid SPEN sequence assayed, incorporating an initial slice selection, a readout k-space axis and a spatiotemporally encoded (SPEN) dimension. The RF/ADC line displays both the RF pulses and the timing of the FID acquisitions (ADC for analog-to-digital converter); the G_{RO}, G_{SPEN}, and G_{SS} rows display the gradients applied along the readout, the spatiotemporally encoded and the slice-selective directions, respectively. Main parameters of the scans: T_{acq}, G_{acq}—acquisition duration and gradient strength associated to the hybrid spectroscopic/SPEN dimension; T_{ro}, G_{ro}—acquisition duration and gradient strength associated with the orthogonal k-space readout dimension; N_{lines}—number of SPEN-encoded elements; T_{180}, G_{180}—chirped pulse duration and associated gradient strength; k_{ro} and k_{SPEN}—pairs of prewinding gradients flanking the adiabatic 180° inversion and imparting $\approx \gamma G_{ro} T_{ro}/4$ and $\approx \gamma G_{180} T_{180}/4$ encodings respectively; G_{cr} and G_{sp}—pairs of crusher and spoiler gradients applied on all axes.

- the benefits that arise by ensuring that the remaining gradient, sweep and timing parameters are chosen so as to achieve a full excitation of the targeted FOV despite of the shielding offsets, that the $\left(1 - \frac{G_{acq}}{2G_{180}}\right)$ shift scaling factors is not too small, that appropriate choices are made for the amplitude and the central frequency of the chirped pulses, and that any a priori information available (like the chemical sites' relative displacements) is used in the reconstruction data processing.

- the limitation of the sequence's site-separation abilities to ΔB_o field inhomogeneity distortions, which by imposing a corresponding $\left(1 - \frac{G_{acq}}{2G_{180}}\right)\gamma \Delta B_o$ line broadening will prevent the resolution of inequivalent sites unless their similarly scaled $\left(1 - \frac{G_{acq}}{2G_{180}}\right)\Delta \nu$ shift differences exceeds this value.

Materials

Besides numerical corroborations of the new procedures here introduced, experiments were conducted to test the method's ability to provide multislice 2D spatial images of chemically distinct species in a single shot. Among the conditions assayed were measurements on phantoms containing various chemical sites at differing concentrations. These experiments were carried out at 7 T on a Varian VNMRS vertical microimaging system. The feasibility and advantages associated with the SPEN-based chemical shift imaging were also examined with a series of in vivo experiments, using two different platforms. Experiments on mice were conducted at 7 T on a Varian VNMRS vertical imaging system using a quadrature-coil Millipede® probe with FOVs of $30 \times 30 \times 46$ mm³. These experiments were performed on the abdominal region, which contains a relative high fat content. These in vivo experiments, as well as all associated animal handling proce-

dures, were done in accordance with protocols approved by the Weizmann Institute's Animal Care and Use Committee. A second set of experiments focused on female human volunteers, were conducted on a 3T Siemens TIM TRIO clinical system using a 4-channels breast coil. This set of experiments sought to verify our new method's ability to separate fat- from water-based (i.e., connective tissue) images in breast and were performed according to procedures approved by the Internal Review Board of the Wolfson Medical Center (Holon, Israel) after obtaining informed suitable written consents.

All the SPEN pulse sequences used in this work were custom written. For the Varian-based experiments RF pulses and gradient shapes were designed in MATLAB® (The MathWorks, Inc., Natick, MA) and uploaded onto the scanner; in the Siemens-based experiments, RF pulses and gradient waveforms were mostly based on available Siemens software. Images were reconstructed in all instances using custom-written MATLAB packages, which included the possibility to process hybrid SPEN-/k-space data with/without SR along the spatiotemporal dimension, and Fourier transformation along the k-dimension. Following Ref. 22, manipulations in the SR data processing included the alignment of positive and negative readout echoes; zero-filling, weighting and other conventional procedures were included in the procedure described earlier, as needed.

RESULTS

Figure 4 investigates the potential spectroscopic and imaging performance benefits that may arise from the new chemical-shift/imaging SR-based SPEN resolution procedure introduced in the preceding section. Toward this end, the sequence of Figure 3 was used to collect a single-slab signal arising from a phantom made up by a 5-mm water tube and a 5-mm cyclohexane tube, both
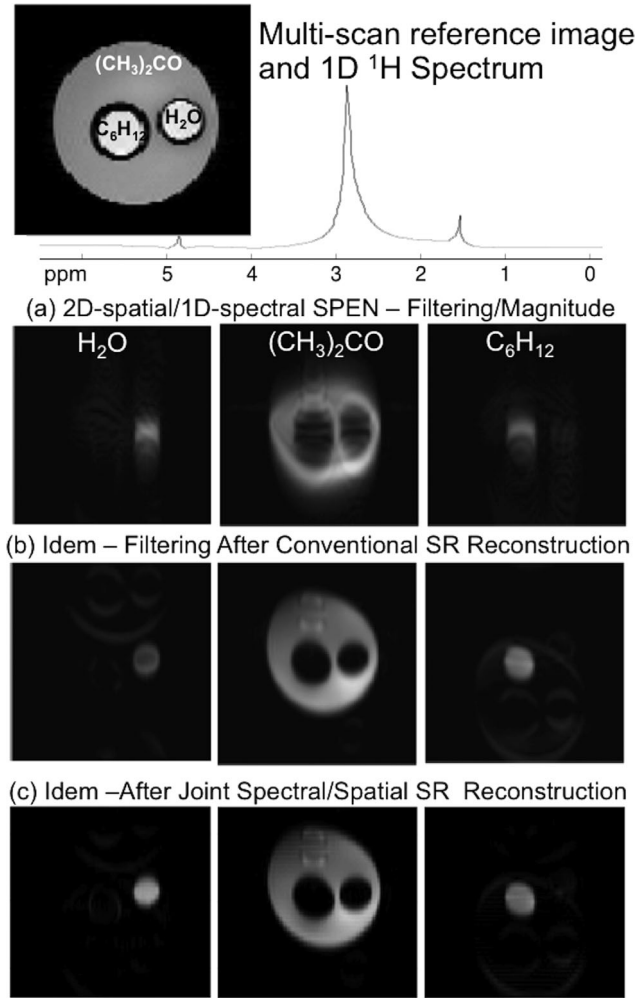
FIG. 4. Single-scan separation of 1D spectral + 2D spatial images, collected using the Hybrid SPEN sequence introduced in Figure 3 and processed by different means. The phantom involved a 5-mm water, a 5-mm cyclohexane, and a 20-mm acetone tubes, physically arranged as indicated in the upper left image and leading to the spectrum shown on the upper-right trace. Panels (**a**)–(**c**) illustrate the results afforded by the different reconstruction methods on the same single-scan experimental data set, collected using a FOV = 30×30 mm^2, a slice thickness = 2 mm, an in-plane effective resolution = 0.33×0.21 mm^2, a T_{180} = 2 ms, G_{180} = 2 G/cm, T_{acq} = 73 ms, and ≈150 ms total acquisition time. All these images are displayed using a common grayscale. The resolution of both spatial dimensions for each chemical site image in (a) is 5.93 mm; it is estimated to be under 0.5 mm in (b) and in (c) due to the avoidance of the shift filtering. Parameters for the multiscan gradient-echo image on the top left: 0.12×0.31 mm^2 in-plane resolution, echo time = 2.9 ms, pulse repetition time = 6 s, and total scan duration = 14 min.

of which were placed inside a 20-mm tube filled with acetone. The resulting single-shot data were then processed by three different ways: using a spectral-filtering/magnitude-imaging calculation akin to that introduced in Ref. 21 (suitably modified to account for the use of a 180° adiabatic sweep instead of a chirped 90° RF imparting the encoding); using a straight image-oriented SR procedure like the one introduced in Ref. 22 (which ignores any a priori information on chemical

shifts) followed by a spectral FT, filtering of the identified peaks and inverse Fourier calculations of the corresponding images; and using the extended-SR-based spectroscopic imaging procedure summarized by the matrix in Figure 2, taking into account both the spatial and the spectral nature of the experiment. In all cases, the results of these procedures managed to resolve the three peaks making up the phantom, with the stronger peak acetone placed in the 20-mm tube and resonating at ≈3 ppm clearly visible, flanked by smaller water (4.8 ppm) and cyclohexane (1.8 ppm) resonances from the 5-mm tubes (top panel in Fig. 4). The imaging performances of the various processing procedures, however, differ from one another: the highest spatial blurring arises, as expected, for a simple magnitude calculation of the filtered peaks (Fig. 4a); resolution is much improved by a purely spatial SR procedure (Fig. 4b); and the extended spectral/spatial SR procedure introduced in this work yields the sharpest spatial resolution and minimal cross-talking among the images arising from the various chemically inequivalent sites (Fig. 4c).

Whereas the phantom used in Figure 4 exemplifies the single-shot 1D spectral/2D imaging abilities of the new extended SR processing algorithm, the images in Figure 5 illustrate the new sequence's ability to efficiently tackle a third spatial axis via multislicing and to probe, even in such multislicing mode, concentrations of the kind normally associated with (abundant) metabolites. This phantom's arrangement is sketched in Figure 5's left-hand side and is made up by aqueous solutions of 99.9% D$_2$O (i.e., ≈110 mM in HDO), 25 mM of choline in D$_2$O, and 100 mM sodium pyruvate in D$_2$O—all placed in three independent 5-mm tubes and centered at different heights within our microimaging probe's 4.5-cm vertical FOV. Three 3-mm-thick slices were then subsequently excited at z-positions separated by 3 mm each and encoded by the sequence introduced in Figure 3, leading to the three sets of 1D spectral/2D spatial data in Figure 5c being collected within a 371-ms total time. The abilities of the sequence/processing combination to resolve the different axial positions of the HDO peak arising from all tubes at 4.8 ppm, and from the 1H methyl peaks of choline (3.2 ppm) and pyruvate (2.4 ppm), are clear. The separation of all chemical sites is satisfactory, and only small spatial artifacts arise despite the relatively low concentrations of the various species.

Figure 6 extends these investigations to animal experiments targeting the inferior abdomen of a mouse. This region was chosen because of its relative high and well-defined fat content. Reference multiscan gradient echo images were also scanned in the same location; once exciting all chemical sites, and a second time incorporating water suppression to highlight the fat-rich regions and enable a straightforward comparison with the single-shot reconstructions. The figure illustrates the abilities of the new single-shot sequence and of its associated SR-processing procedure to deal also appropriately with such cases: spatial features are faithfully reproduced for both components and the cross-talk between the two contributing spectral signals is minimal.

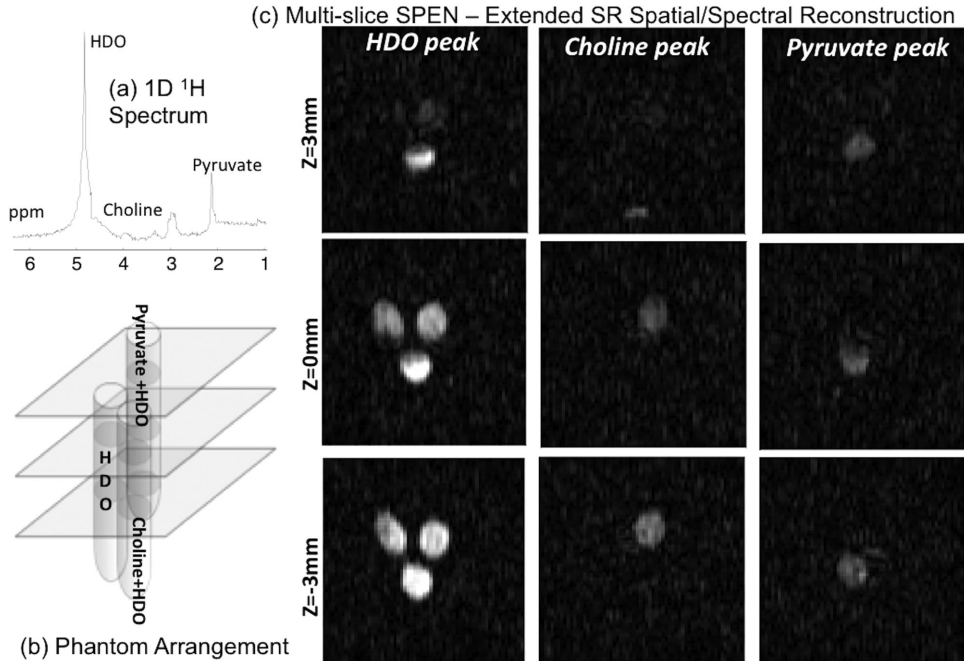The above example, executed at 7 T, involved a fat/water separation of ~1000 Hz. To explore the method's

FIG. 5. Multislice SPEN spectroscopic imaging results obtained for HDO (protonated water diluted by heavy water) at ≈110 mM (4.8 ppm, present in all tubes), choline (25 mM, with only the methyl protons visible at ≈3.2 ppm), and sodium pyruvate (100 mM, methyl protons at 2.4 ppm). **a**: Phantom's 1D ^{1}H spectrum. **b**: Cartoon showing the tubes' locations. **c**: 2D spatial images reconstructed for different z-slices (from top to bottom) and for each chemical site (from left to right). Scan parameters: FOV = 30 × 30 mm^2; in-plane effective resolution = 0.67 × 0.43 mm^2; T_{180} = 2 ms; G_{180} = 2 G/cm; T_{acq} = 73 ms; # of slices = 3; slice thickness = 3 mm; total scan duration = 371 ms. All images are displayed using a common grayscale; the noise appearing as white stripes/dots in these images reflect the limited sensitivity of these single-scan metabolite-oriented images.

ability to deal with the smaller spectral peak separations and more heterogeneous distributions expected in human analyses, the method was assayed at 3 T with a series of breast imaging scans on female volunteers. Spectroscopic magnetic resonance imaging studies are then complicated by the smaller chemical shift difference between the sites (≈450 Hz), as well as by the relatively higher environmental inhomogeneities that are known to characterize breast imaging (24,25). Figure 7 presents both coronal and axial imaging results, comparing for each plane the (a) fat- and water-only 2D multiscan reference images that can be obtained by conventional gradient-echo methods (for the coronal scan the separate fat and water displays were prepared by threshold segmentation of the full multiscan image), against the single-shot 1D spectral/2D spatial images arising for the same slice from (b) the original filtering/magnitude calculation of Ref. 21, and (c) from the new extended-SR formulation of this SPEN-based single shot data. Both single-shot approaches yield images that show reasonable agreement with the spectrally selective multiscan data; still, the new SR-based method yields superior faithfulness and resolution for both axial and coronal cuts than its simpler filtering/magnitude-calculation counterpart (especially for the low chirp rate pulses that in human experiments have to be used to reduce the exams SAR).

As an additional investigation on the abilities of this SR-based version of SPEN to yield 3D spatial/1D spectral data, we compare in Figure 8 the multislicing performance of the new method, against conventional multishot, multislice

phase-encoded experiments used as references. The figure exhibits a quality reconstruction of the respective chemical site's images for all five slices targeted by the method, despite the nearly 200× acceleration factor involved.

DISCUSSION AND CONCLUSIONS

The measurements presented in this study validate the use of SPEN-based techniques as valuable additions to the existing toolkit available to reconstruct spectrally resolved 3D images in a subsecond fashion. Previous studies had alluded to SPEN's unique mode of conveying chemical shift information by exploiting a phase modulation that is not fully used or needed by the image-reconstruction procedure. This redundancy leads to a considerable simplification in the pulse sequence's complexity vis-à-vis alternatives that, like EPSI, require an additional nested gradient oscillation to retrieve comparable spectral/spatial information. Still, these previous implementations brought this advantage to bear by spectral filtration procedures that involved certain compromises in the ensuing spatial resolution and/or spectral cross-talk effects. These effects are here superseded thanks to an extended SR formulation that exploits both the relatively small number of distinct chemical sites involved in MRSI and the well-defined nature of the SPEN-based imaging reconstruction algebra, into a single, noniterative, highly stable reconstruction procedure. The ensuing spectroscopic data displays high spectral resolution and spatial definition; comparisons against suitably shift-suppressed EPI counterparts also
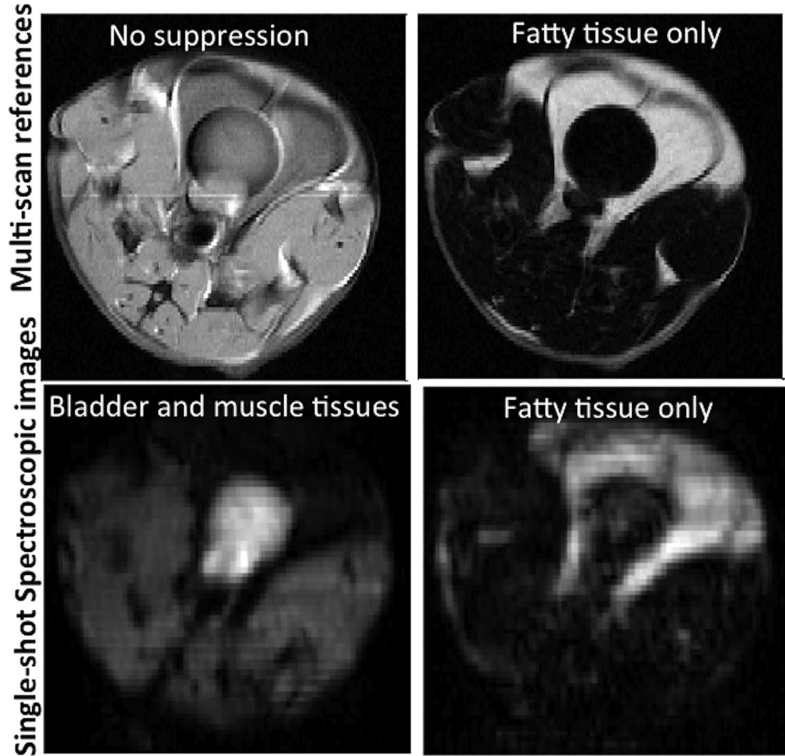
FIG. 6. In vivo fat/water separation capabilities of the SPEN methodology introduced in "Methods" section, as applied to abdominal mouse investigations at 7 T. Top: Multiscan references involving no suppression on the left and water-suppression on the right. Common parameters of these images: FOV = 30×30 mm^2, resolution = 0.12×0.23 mm^2, slice thickness = 2 mm, andscan duration = 8 s. Bottom: Fat- and water-tissue images separated for the same 2-mm z-slab by the expanded SR procedure. Left hand: water-signal contribution; right-hand: fat-signal contribution. Single scan acquisition parameters: FOV = 25×25 mm^2, in-plane effective resolution = 0.35×0.35 mm^2, T_{acq} = 30.8 ms, T_{180} = 2 ms, G_{180} = 6 G/cm, and total scan duration = 50 ms.
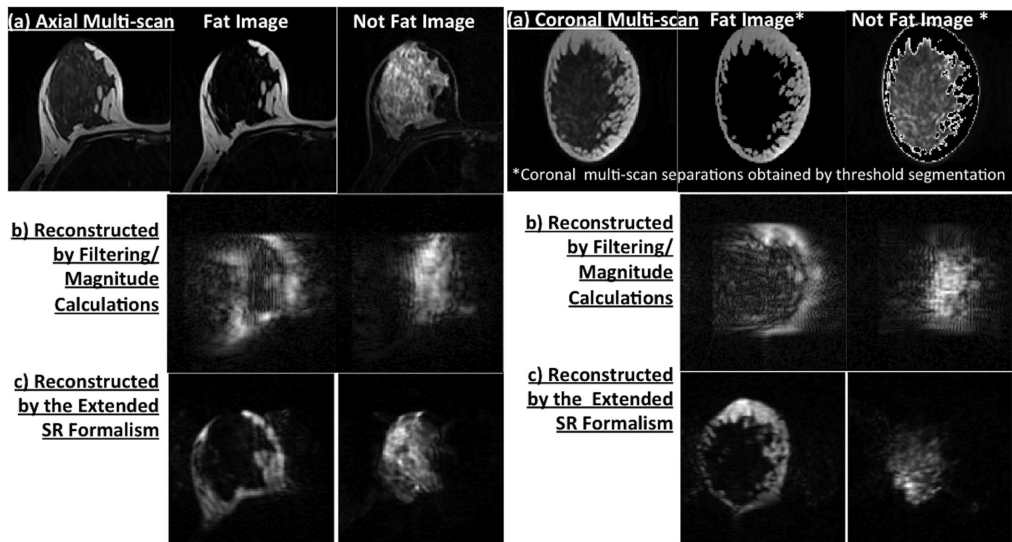

FIG. 7. Axial (left) and coronal (right) scan comparisons on a healthy breast imaging volunteer. **a**: Multishot reference with both chemical sites separated by selective excitation of the respective peaks for the axial case, and separation by threshold segmentation for the coronal scan. Acquisition parameters: FOV = 32×32 cm^2 (only left breast shown), resolution = 0.8×0.8 mm^2, slice thickness = 2.5 mm, scan duration 35 s. **b,c**: Single-scan Hybrid SPEN results obtained upon processing the same data set using the spectral resolution procedure described in Ref. 21 (center), and the extended-SR formulation of this work (bottom). Common experimental parameters for (b,c): FOV = 20×20 cm^2, slice thickness = 2.5 mm, T_{acq} = 108 ms, T_{180} = 5.8 ms, G_{180} = 0.12 G/cm, single slice scan duration 170 ms. In-plane effective resolution was 2.5×1.0 mm^2 for the coronal scan and 2.0×1.33 mm^2 for the axial one.
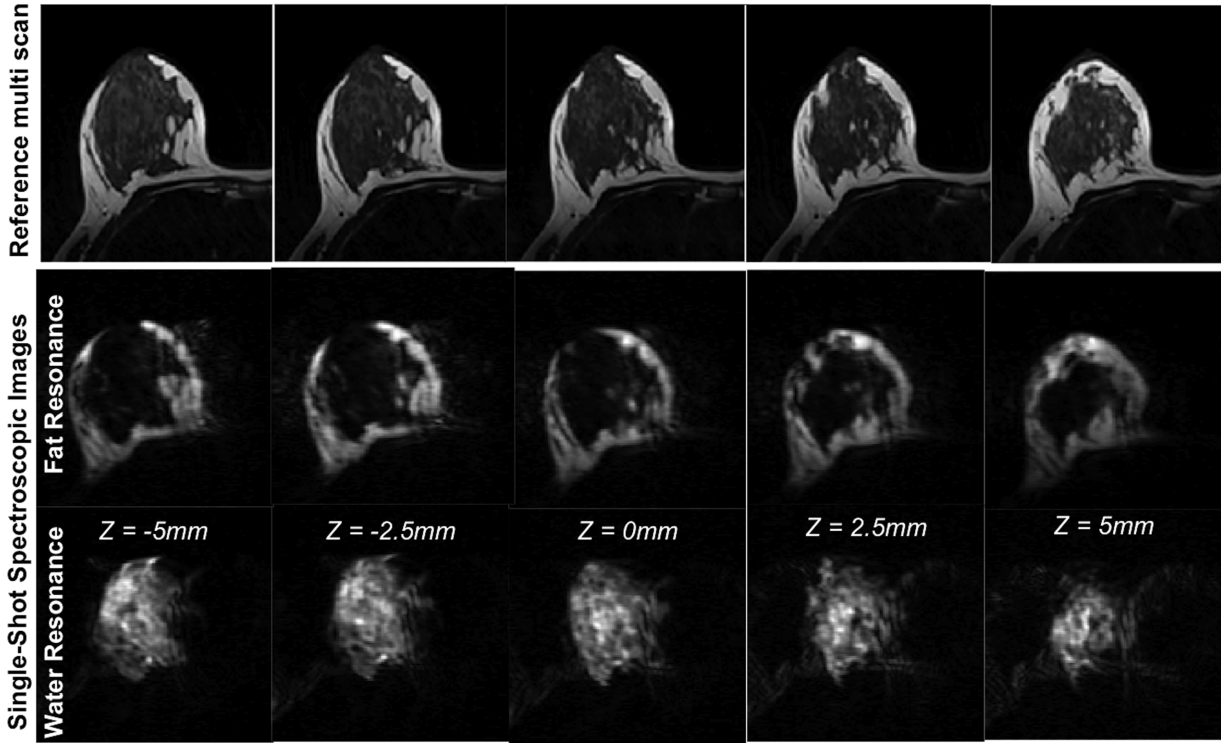
FIG. 8. Comparison between five slices collected by a conventional multiscan gradient echo sequence (top), against the two spectroscopically resolved images afforded by the SPEN-based procedure of Figure 3 for the indicated slices and chemical shift. Multiscan parameters: FOV = 32×32 cm^2 (only left breast shown), resolution = 0.8×0.8 mm^2, slice thickness = 2.5 mm, and scan duration = 35 s. Single-shot SPEN parameters: FOV = 20×20 cm^2, in-plane effective resolution = 2.0×1.33 mm^2, slice thickness = 2.5 mm, T_{acq} = 108 ms, T_{180} = 5.8 ms, G_{180} = 0.12 G/cm, and total multislice scan duration = 850 ms.

demonstrate the method's good sensitivity—within the natural limits of single-scan approaches that typically forgo the signal-to-noise improvements associated with extensive signal averaging. For example, optimized tests performed on a simple phantom containing an inner water tube surrounded by a larger oil tube, afforded spin-echo EPI water images (incorporating "oil suppression") displaying ca. 2/3 of the signal-to-noise ratio obtained upon executing the sequence in Figure 3 with similar acquisition and resolution parameters. Moreover, such comparison factors neither in the smaller spatial distortions displayed at the oil/water interface by the latter experiments
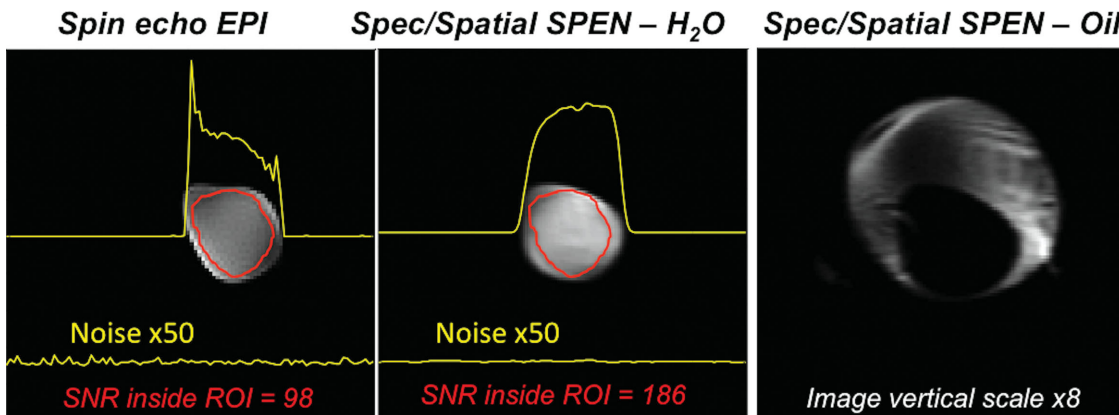

FIG. 9. Comparison between a 3T spin-echo EPI (left) and single-scan spectroscopic SPEN images (center/right) collected on the same phantom, consisting of a $\approx$6-cm diameter water specimen inside an oil-containing $\approx$12-cm diameter tube. To compare relative sensitivities these two experiments examined identical 5-mm slices—using a "fat-suppression" presaturating pulse in the EPI case and the site-resolving SR protocol introduced in this study for the SPEN images—were excited, and the ratios between the average water signals afforded by the regions indicted in red and the noise arising upon subtracting two identical fully relaxed scans, were calculated. Traces at and below the highlighted regions illustrate cross-sections of signal and noise traces (taken at the indicated positions); the ensuing signal/noise ratios are indicted under the images. Notice that in addition to a $\geq$50% higher sensitivity, SPEN provides an oil image from the same experiment (right), as well as a higher robustness as evidenced by the "rounder," more uniform water profile. Other acquisition parameters: FOV = 20×20 cm^2, resolution = 2.0×1.3 mm^2, acquisition times = 104 ms, T_{180} = 5.8 ms, and G_{180} = 0.12 G/cm.

nor in the additional "fat" image that the SPEN experiments afforded in the same single scan (Fig. 9). A mathematical description explaining the higher sensitivity usually exhibited by super-resolved SPEN images over their EPI-based counterparts is currently under development.

A new throughput-related issue addressed by this work involves a multislice operation, which was here achieved by a suitable combination of frequency-swept and of hard 180° pulses—instead of the single 90° chirped pulse of our original proposition. When incorporating the SR-based reconstruction the resulting sequences afforded high resolution and repetition rates, without having to confront challenges associated to excessive RF-driven power depositions. Further advantages and improvements in the experiment's spatial resolution can result by incorporating multichannel, multicoil parallel imaging information—both along the slice-selected axes and along the SR-processed SPEN dimension. In the latter instance, customized excitation modes can be proposed that maximize speed and spatial resolution, as will be detailed in an upcoming publication.

In terms of applications, main emphases were here placed on the method's ability to provide well-resolved fat and water single-shot multislice images, as well as to discern the images of concentrated metabolites in a single scan at relatively high spatial resolutions. The resulting methods could surely find valuable applications, not only for breast imaging but also for characterizing other fatty tissues—particularly those involved in organs that due to breathing, pulsation or beating, experience substantial motions like liver and kidney (26,27). Another important direction where this method can be found valuable is when dealing with dynamic imaging, including metabolic hyperpolarized applications (28,29). Albeit arguably more challenging, the approach also opens new opportunities worth exploring in relation to functional MRSI studies. In such instances, regularization and/or deconvolution procedures (none of which were here assayed) could yield the further sensitivity improvements that will surely be then needed to confront the sensitivity challenges expected to arise even at the highest fields. Research in all these areas is currently in progress.

ACKNOWLEDGMENTS

REFERENCES

1. Brown T, Kincaid B, Ugurbil K. NMR chemical shift imaging in three dimensions. Proc Natl Acad Sci USA 1982;79:3523–3526.
2. Posse S, DeCarli C, Le Bihan D. Three-dimensional echo-planar MR spectroscopic imaging at short echo times in the human heart. Radiology 1994;192:733–738.
3. Kurhanewicz J, Vigneron DB, Nelson SJ. Three-dimensional magnetic resonance spectroscopic imaging of brain and prostate cancer. Neoplasia 2000;2:166–189.
4. Clayton DB, Elliott MA, Lenkinski RE. In vivo proton spectroscopy without solvent suppression. Concepts Magn Reson 2001;13:260–275.
5. Nelson SJ. Magnetic resonance spectroscopic imaging. Evaluating responses to therapy for gliomas. IEEE Eng Med Biol Mag 2004;23:30–39.
6. Cunningham CH, Chen AP, Albers MJ, Kurhanewicz J, Hurd RE, Yen Y, Pauly JM, Nelson SJ, Vigneron DB, Double spin-echo sequence for rapid spectroscopic imaging of hyperpolarized ^{13}C. J Magn Reson 2007;187:357–362.
7. Larson PEZ, Hu S, Lustig M, Kerr AB, Nelson SJ, Kurhanewicz J, Pauly JM, Vigneron DB, Fast dynamic 3D MR spectroscopic imaging with compressed sensing and multiband excitation pulses for hyperpolarized 13C studies. Magn Reson Med 2011;65:610–619.
8. Kurhanewicz J, Vigneron DB, Brindle K, et al. Analysis of cancer metabolism by imaging hyperpolarized nuclei: prospects for translation to clinical research. Neoplasia 2011;13:81–97.
9. Maudsley A, Hilal S, Perman W, Simon H. Spatially resolved high resolution spectroscopy by four-dimensional NMR. J Magn Reson 1983;51:147–152.
10. Mansfield P. Multi-planar image formation using NMR spin echoes. J Phys C: Solid State Phys 1977;10:55–58.
11. Mansfield P. Spatial mapping of the chemical shift in NMR. Magn Reson Med 1984;1:370–386.
12. Adalsteinsson E, Irarrazabal P, Topp S, Meyer C, Macovski A, Spielman D. Volumetric spectroscopic imaging with spiral-based k-space trajectories. Magn Reson Med 1998;39:889–898.
13. Van der Zwaag W, Francis S, Bowtell R. Improved echo volume imaging (EVI) for functional MRI. Magn Reson Med 2006;56:1320–1327.
14. Pohmann R, von Kienlin M, Haase A. Theoretical evaluation and comparison of fast chemical shift imaging methods. J Magn Reson 1997: 129:145–160.
15. Pruessmann KP, Weiger M, Scheidegger MB, Boesiger P. SENSE: sensitivity encoding for fast MRI. Magn Reson Med 1999;42:952–962.
16. Reeder SB, Brittain JH, Grist TM, Yen Y-F. Least-squares chemical shift separation for ^{13}C metabolic imaging. J Magn Reson Imaging 2007;26:1145–1152.
17. Reeder SB, McKenzie CA, Pineda AR, et al. Water-fat separation with IDEAL gradient-echo imaging. J Magn Reson Imaging 2007;25:644–652.
18. Kunz D. Use of frequency-modulated radiofrequency pulses in MR imaging experiments. Magn Reson Med 1986;3:377–384.
19. Pipe JG. Spatial encoding and reconstruction in MRI with quadratic phase profiles. Magn Reson Med 1995;33:24–33.
20. Shrot Y, Frydman L. Spatially-encoded NMR and the acquisition of 2D magnetic resonance images within a single scan. J Magn Reson 2005;172:179–190.
21. Tal A, Frydman L. Spectroscopic imaging from spatially-encoded single-scan multidimensional MRI data. J Magn Reson 2007;189:46–58.
22. Ben-Eliezer N, Irani M, Frydman L. Super-resolved spatially-encoded single-scan 2D MRI. Magn Reson Med 2010;63:1594–1600.
23. Ben-Eliezer N, Frydman L. Spatiotemporal encoding as a robust basis for fast three-dimensional in vivo MRI. NMR Biomed 2011;24:1191–1201.
24. Englander SA, Ulüg AM, Brem R, Glickson JD, van Zijl PCM Diffusion imaging of human breast. NMR Biomed 1997;10:348–352.
25. Henry-Tillman RS, Harms SE, Westbrook KC, Korourian S, Klimberg VS. Role of breast magnetic resonance imaging in determining breast as a source of unknown metastatic lymphadenopathy. Am J Surg 1999;178:496–499.
26. Rosen BR, Carter EA, Pykett IL, Buchbinder BR, Brady TJ. Proton chemical shift imaging: an evaluation of its clinical potential using an in vivo fatty liver model. Radiology 1985;154:469–472.
27. Sijens PE, Edens MA, Bakker SJL, Stolk RP. MRI-determined fat content of human liver, pancreas and kidney. World J Gastroenterol 2010;16:1993–1998.
28. Larson PEZ, Bok R, Kerr AB, Lustig M, Hu S, Chen AP, Nelson SJ, Pauly JM, Kurhanewicz J, Vigneron DB. Investigation of tumor hyperpolarized [1–13C]-pyruvate dynamics using time-resolved multiband RF excitation echo-planar MRSI. Magn Reson Med 2010;63:582–91.
29. Hu S, Lustig M, Chen AP, Crane J, Kerr A, Kelley DAC, Hurd RE, Kurhanewicz J, Nelson SJ, Pauly JM, Vigneron DB. Compressed sensing for resolution enhancement of hyperpolarized 13C flyback 3D-MRSI. J Magn Reson 2008;192:258–264.